



4D printed continuous fiber reinforced shape memory polymer composites with enhanced mechanical properties and shape memory effects

Chengjun Zeng^a, Liwu Liu^a, Cheng Lin^b, Xiaozhou Xin^a, Yanju Liu^{a,*}, Jinsong Leng^b

^a Department of Astronautical Science and Mechanics, Harbin Institute of Technology (HIT), No. 92 West Dazhi Street, PO Box 301, Harbin 150001, People's Republic of China

^b Center for Composite Materials and Structures, Harbin Institute of Technology (HIT), No. 2 Yikuang Street, Harbin 150080, People's Republic of China

ARTICLE INFO

Keywords:

- A. Smart materials
- A. Polymer-matrix composites (PMCs)
- B. Mechanical properties
- E. 3-D Printing

ABSTRACT

Multi-material four-dimensional (4D) printing has gathered significant interest among researchers as an emerging manufacturing technique. In this study, continuous carbon fibers are integrated into shape memory polymers (SMPs) using multi-material co-extrusion 4D printing. This process results in the creation of shape memory polymer composites (SMPCs) characterized by high load-bearing capacity and stimulus responsiveness. Micro-CT scanning is employed to evaluate the internal porosity of SMPCs, based on which the three-dimensional (3D) reconstruction images are generated. Meanwhile, various mechanical tests are implemented, including tensile, three-point bending, and compression tests, to explore the mechanical properties and fracture modes of the 4D printed SMPCs. In addition, the shape memory effect of the 4D printed SMPCs is verified by experiments and finite element simulations. The results demonstrate shape recovery rates higher than 96%. This study offers valuable insights into the fabrication and testing of smart composites with compatible deformation and high load-bearing capacity.

1. Introduction

Additive manufacturing, or three-dimensional (3D) printing, is widely regarded as a disruptive technique poised to transform advanced manufacturing industries in the future [1–3]. This technique enables the rapid integration of 3D structures with complex geometries [4,5]. Initially, 3D printing found applications in fields like biomedicine [6], flexible electronics [7,8], intelligent robotics [9], and space science [10]. Traditionally, the advantages of 3D printed components over those prepared by conventional processes have primarily been associated with geometric complexity and shorter production cycles, with limited focus on functionality and applicability [11]. However, the emergence of smart and programmable materials that can respond to external stimuli has opened up new possibilities in the realm of 3D printing [12–15]. By combining 3D printing technique with these materials, the concept of four-dimensional (4D) printing was introduced [16,17]. In contrast to traditional 3D printing, 4D printing introduces an additional dimension, i.e., time. This allows 3D printed components to alter their shape or function in response to external stimuli such as heat, light, electricity, solution, or magnetic fields [18,19].

Shape memory polymers (SMPs) are smart materials that can recover

from a temporary configuration to a pre-designed shape when subjected to external stimuli [20–23]. These materials have been extensively applied in 4D printing, where they enable the creation of structures that can change over time. Researchers have developed various SMP systems that boast high deformability and fatigue resistance, as well as compatibility with 3D printing techniques [24,25]. These SMP systems facilitate the production of intricate, high-resolution structures and mechanical metamaterials with properties that mimic biological materials in terms of their stress–strain responses under significant deformation [26]. Advances in 4D printing have also led to the formulation of specialized SMP inks that support rapid prototyping of microscale structures [27]. The utility of SMPs extends to the fabrication of active components like self-folding hinges and intelligent origami metamaterials that can undergo shape transformation and modulate their mechanical properties in response to thermal stimuli, highlighting the potential for SMPs to revolutionize the design of responsive, adaptable materials and devices [28,29].

As mentioned above, considerable progress has been achieved in the research of 4D printed SMPs. However, most 4D printed SMP structures face a common challenge in their deficiency in meeting the high mechanical properties and multi-drive characteristics required for load-

* Corresponding author.

E-mail address: yj_liu@hit.edu.cn (Y. Liu).

bearing or multifunctional components [30,31]. The emergence of multi-material 4D printing has addressed this issue, with several functional long fibers being utilized as reinforcements in the 4D printing of SMPs to fabricate multifunctional and high-strength SMP composites (SMPCs) [32–40]. For example, Zeng et al. prepared SMPCs with outstanding flexural properties and an electro-induced shape memory effect using continuous carbon fibers and SMP via a melt co-extrusion 4D printing process [34]. Le Duigou et al. proposed a novel 4D printed multi-stimulus responsive composite that combines continuous carbon fibers with moisture-sensitive polymers, following for autonomous deformation triggered by alternations in ambient humidity or electric heating [35]. Similarly, Zhou et al. also reported a co-extrusion 4D printing strategy that integrates continuous metal fibers into thermoplastic SMPs, establishing an electrically heated path in the polymer matrix [33]. Despite the progress in researching 4D printed continuous fiber-reinforced SMPCs, there remains a need for systematic characterization efforts to reveal the information regarding the internal defect distribution, tensile/compression/bending mechanical properties, and shape memory behavior of these materials.

In this study, a fiber/polymer in-situ impregnation co-extrusion 4D printing process is employed to fabricate continuous fiber-reinforced SMPCs. After that, the internal defect distribution, surface morphology, tensile/bending/compression properties, and shape memory properties of the 4D printed SMPCs are investigated comprehensively. Specifically, the internal defect distribution of SMPCs is characterized by harnessing micro-CT scanning. The systematic tensile, three-point bending, and compression tests are carried out to evaluate the mechanical properties. The surface morphology of specimens after failure is scrutinized using scanning electron microscopy (SEM) to reveal their failure mechanisms under various loading modes. Additionally, the shape memory effect of these materials is evaluated by shape recovery tests. Furthermore, a constitutive model that is compatible with the finite element software ABAQUS is used to predict their shape memory response.

2. Experimental section

2.1. Materials

The raw materials utilized to prepare the continuous fiber-reinforced SMPCs include poly(lactic acid) (PLA)-based SMP and continuous carbon fibers, with PLA consumables being supplied by the Harbin Institute of Technology [41]. PLA-based SMP is characterized as a semi-crystalline polymer, possessing amorphous and crystalline regions within its polymer chains, thus demonstrating shape memory effects when subjected to specific temperature stimuli. Consequently, the 3D printed PLA structures exhibit active deformation (4D transformation) when exposed to elevated temperatures.

The dynamic thermomechanical properties of PLA-based SMP are assessed through tensile mode, utilizing a dynamic thermomechanical analyzer (TA Instrument, DMA Q800). The DMA results of PLA-based SMP, as illustrated in Fig. 1a, indicate an inverse S-shaped evolution of the storage modulus with increasing temperature. This behavior implies that PLA-based SMP is a thermotropic variable stiffness material. The low modulus in the high-temperature range facilitates the shape programming of SMP components. In addition, the glass transition temperature (T_g) of approximately 67 °C is determined from the peak of the loss tangent curve, signifying that the shape recovery test should be performed in an environment close to or exceeding this temperature. The continuous carbon fibers utilized in this experiment are Toray carbon fiber bundles (T300B-1000), comprising 1,000 filaments with a diameter of 7 μm (Fig. 1b).

2.2. Fabrication of 4D printed continuous fiber-reinforced SMPC

The continuous fiber-reinforced SMPC is fabricated using a composite 3D printer (Combot-200, Shaanxi Fibertech Technology Development Co., Ltd., China), designed based on the fiber/polymer in-situ co-extrusion principle (Fig. 1c). Continuous fiber bundles and thermoplastic SMP are fed into the printing nozzle through separate feed channels. Within the nozzle, the thermoplastic SMP will melt and impregnate the fiber bundle, driven by the high-temperature stimulus generated by the heater. Subsequently, the impregnated fiber bundle is extruded from the nozzle and cured on the printing platform (Fig. 1d).

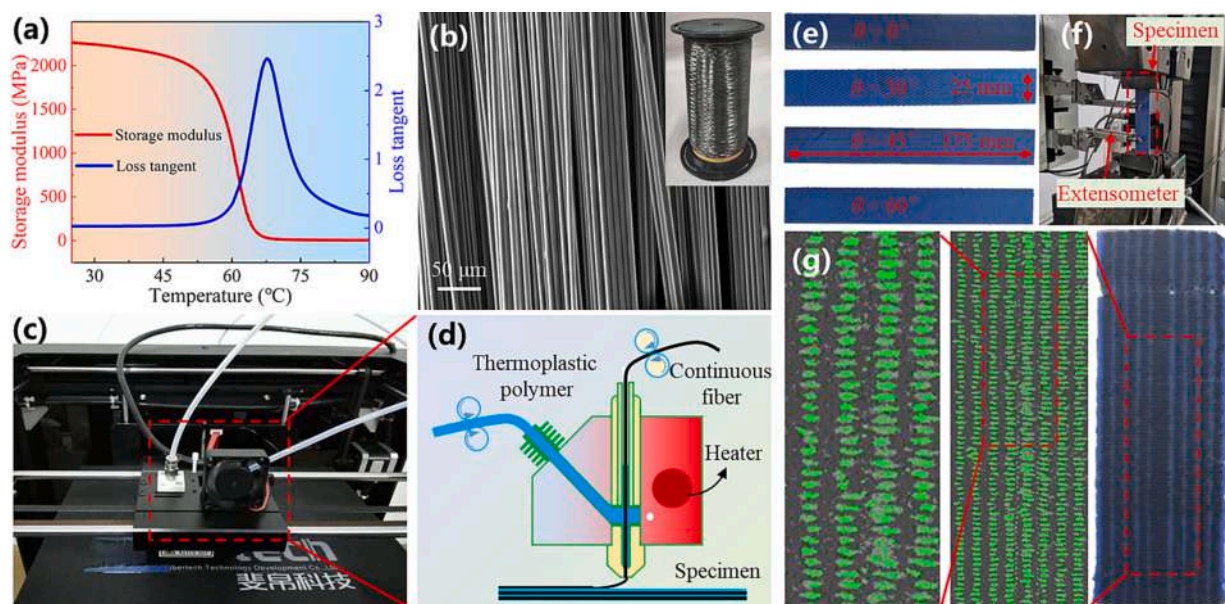


Fig. 1. 4D printed continuous fiber-reinforced SMPC. (a) DMA curve of PLA-based SMPs. (b) Micromorphology of T300B-1000 carbon fiber bundles. (c) 3D printer in a co-extrusion manner for fabricating continuous fiber-reinforced polymer composites. (d) Schematic diagram of in-situ impregnation and co-extrusion of fiber and polymer. (e) Tensile specimens with varying fiber off-axis angles. (f) Tensile testing equipment. (g) Fiber distribution in the cross-section of the specimen.

It's important to note that the composite 3D printer does not employ a fiber shearing mechanism, restricting any abrupt movements or jumps in the nozzle's position during specimen preparation. Due to this limitation, the printing path must be meticulously customized to ensure a continuous nozzle position throughout the moving process. When manufacturing SMPCs through 4D printing, process parameters such as nozzle temperature and printing speed pose a severe impact on the surface quality and mechanical properties of the specimens, and therefore require careful consideration. After multiple validations and optimizations, the following printing parameters are selected: a nozzle diameter of 1 mm, a nozzle temperature of 220 °C, a printing speed of 100 mm/min, and a layer height of 0.3 mm [42]. Moreover, controllable fiber volume fractions within SMPCs are achieved by adjusting the spacing between adjacent deposition lines during the printing process for a constant value of nozzle diameter and layer height. SMPC specimens with various fiber lay-up angles are prepared.

2.3. Mechanical characterization

Uniaxial tensile tests are performed on the 4D printed SMPC specimens with reference to the ASTM D3039/D3039M standard. The tensile specimens are designed with dimensions of 175 mm × 25 mm × 2.4 mm and account for four different fiber off-axis angles, specifically 0°, 30°, 45°, and 60° (Fig. 1e). All specimens possess a consistent fiber volume fraction of 12%. The experimental setup employs a Zwick/Roell Z10 universal testing machine, complemented by an electronic extensometer for real-time strain measurements of specimens (Fig. 1f). Throughout the test, the constant strain rate is set to 0.001/s.

The bending specimens are designed following the ASTM D7264/D7264M-15. The nominal dimensions of these specimens are 85 mm × 13 mm × 2.4 mm. Four different fiber off-axis angles such as 0°, 30°, 45°, and 60° are taken into account, while maintaining a consistent fiber volume fraction of 12%. The three-point bending tests are performed with a span of 48 mm and a loading rate of 4.0 mm/min.

To explore the influence of fiber content and loading direction on the compression properties of 4D printed SMPCs, unidirectional fiber-reinforced SMPC specimens with varying fiber volume fractions ($f_f = 12\%$, 19% and 28%) are fabricated following GB/T 1448–2005. Two distinct loading modes are selected for examination: longitudinal and transverse compressions with the loading direction parallel to and perpendicular to the fiber direction, respectively. The size of specimens is 30 mm × 12 mm × 11 mm, and the compression gauge length and compression rate are set to 30 mm and 2 mm/min, respectively.

2.4. Characterization of microstructure and morphology

In this study, surface morphology of the 4D printed SMPCs is characterized using a micro-CT scanner (Phoenix V|tome|x S240, Germany). The dimensions of the specimens are 30 mm × 12 mm × 11 mm. The X-ray settings include a voltage of 100 kV, a current of 120 μA, and a scanning resolution of 17 μm/pixel. The 2D images obtained from scanning are processed for brightness and contrast adjustments using VG Studio software, followed by 3D model construction. Fig. 1g presents the micro-CT images of the specimen's cross-section, providing visibility into the fiber distribution across the cross-sectional area. The fibers on the cross-section are highlighted in green using ImageJ, and the fiber volume fraction of about 12% is obtained statistically. In addition, the morphology of fractured specimens is characterized by SEM (ZEISS SIGMA300).

2.5. Characterization of shape recovery behavior

The shape memory performance of the 4D printed SMPCs is evaluated under bending conditions, considering two SMPC structures: a simple rectangular structure and a complex mesh structure. The test procedures are as follows. Firstly, the specimen is subjected to a bending

moment at 70 °C to bend it by a specific angular deformation (φ). Subsequently, the specimen is cooled down to 25 °C, during which the applied bending moment is removed, effectively preserving its temporary shape. Finally, the specimen is heated to 80 °C to observe the shape recovery process. Furthermore, an anisotropic viscoelastic constitutive model was used to predict the shape memory behavior exhibited by the 4D printed SMPCs. This model is successfully implemented in ABAQUS by writing a user material (UMAT) subroutine. For more comprehensive details regarding model derivation and parameter determination, please refer to our previous work [42].

3. Results and discussion

3.1. Micro-CT images and void characteristics

The presence of a high void fraction inside the material is an inherent limitation of the fused deposition 3D printing technique. This effect is especially pronounced when printing continuous fiber-reinforced polymer composites. Fig. 2 displays the micro-CT images of the 4D printed SMPCs, which provides insights into the void distribution. To facilitate further analysis, a local coordinate system (o - xyz) is defined based on the 3D reconstruction image of the specimen, as depicted in Fig. 2a. By examining the micro-CT images of various surfaces of the specimen, it becomes apparent that voids are prominently rendered in red. On the surfaces parallel to the fiber direction, as shown in Fig. 2b and Fig. 2c, an uneven surface is evident due to resin spillage between the layers. This phenomenon results in the formation of gaps parallel to the fiber direction. Notably, in the x - y plane, the overlap between adjacent deposition lines contributes to the development of stronger non-planar features, increasing the surface porosity.

Fig. 2d presents a microscale view of the surface oriented perpendicular to the fiber direction. Here, voids are classified into intra-bead and inter-bead ones [43]. The intra-bead voids are those inside the carbon fiber bundles formed due to poor impregnation. Their formation is influenced by melt flow characteristics, printing pressure, and impregnation time. On the contrary, the inter-bead voids refer to those between each fiber bundle bead and are mainly caused by the spreading filament structure.

The reconstruction and visualization of voids at different cross-sections inside the 4D printed SMPC are depicted in Fig. 3. Specifically, Fig. 3a exhibits micro-CT images at various y values in the x - z plane. It reveals that voids are distributed along the printing path, forming elongated gaps. This pattern of voids reflects the directional nature of the extrusion process, where material deposition and subsequent fusion between layers may not be seamless, leading to the formation of such gaps. Furthermore, it is important to consider that the observed fiber misalignment, which contributes to the development of concentrated voids in the material matrix, might not solely arise from variations within the extrusion system or from the non-uniform velocities of the nozzle. This phenomenon might also be significantly affected by other factors, such as a mismatch between the fiber bundle diameter and the nozzle aperture, as well as the tension applied to the fibers during the printing process. Notably, in the cross-section close to the upper and lower surfaces of the specimen, voids are distributed more densely, which is confirmed by the porosity statistics in Fig. 3b. The highest porosities are observed in the cross-sections at $y = 2$ mm and $y = 10$ mm. These areas are often subjected to different cooling rates and are more prone to the effects of surface tension and oozing during the printing process, which may account for the increased void presence.

Fig. 3c presents the micro-CT images at different z values (thickness) in the x - y plane, where similar elongated gaps are observed. High porosities are identified in the cross-sections at $z = 10$ mm and $z = 20$ mm. This may have resulted from the undesirable deformation and overlap of fiber filaments during the printing of this layer, as explicated in Fig. 3d. Fig. 3e shows the microscopic images at different x values in the y - z plane. The images expose an uneven dispersal of intra-bead voids, which

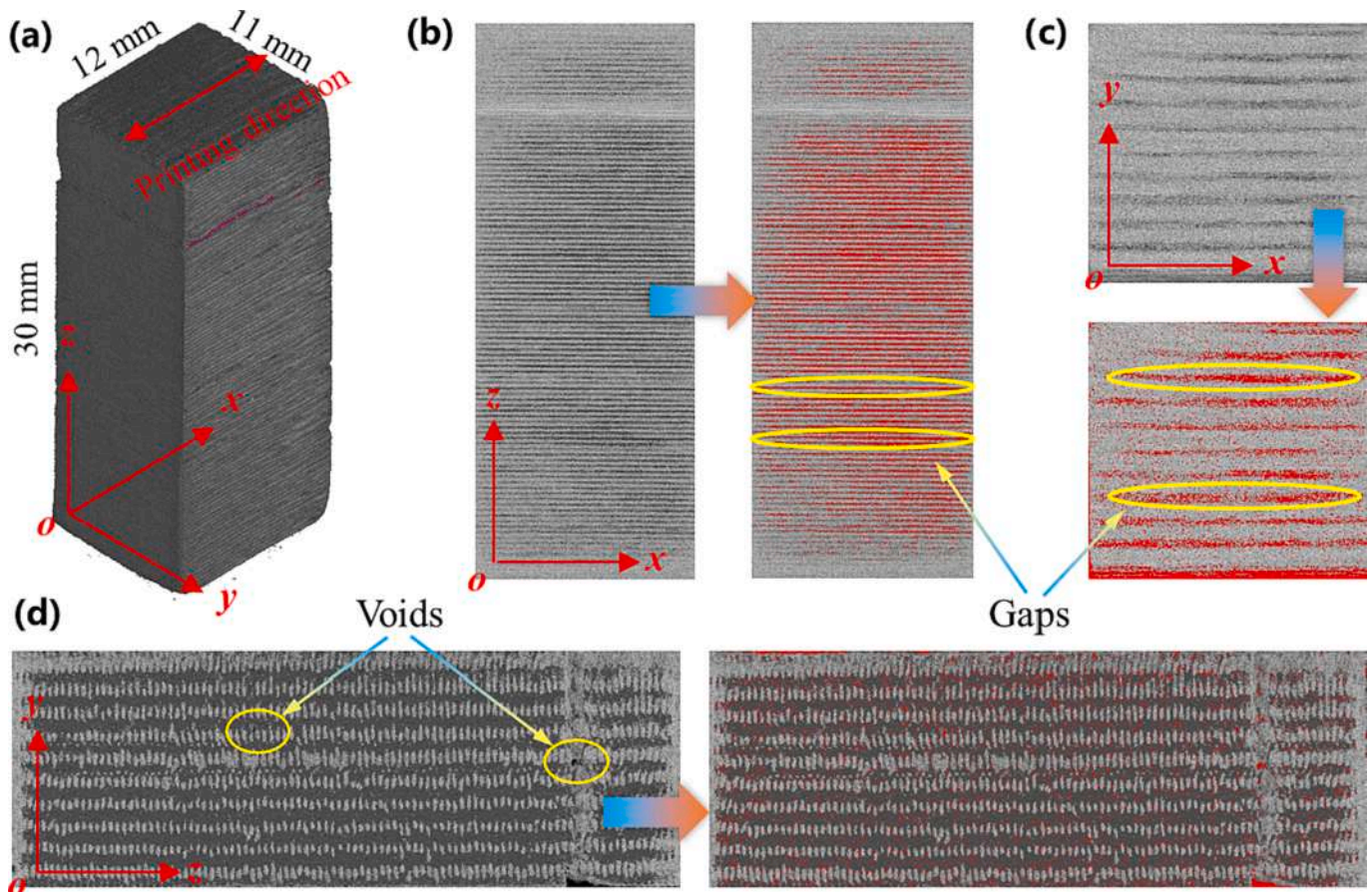


Fig. 2. Micro-CT images of (a) 3D reconstruction, (b) x - z plane, (c) x - y plane, and (d) y - z plane for 4D printed SMPCs.

are predominantly situated along the peripheral regions of the specimen. These voids also demonstrate a reduced scale, having a lesser length and a more diminutive diameter when contrasted with inter-bead voids. Consequently, porosity in the y - z plane of the specimen is relatively small in contrast to other coordinate cross-sections (Fig. 3f). An examination of the root causes for the asymmetric distribution of the intra-bead voids suggests that it could stem from the fabrication technique employed. Specifically, it may be the result of non-uniform thermal exposure during the printing process, where the exterior of the specimen experiences different cooling rates compared to the interior, consequently leading to a higher concentration of voids at the specimen's edges. Additionally, the deposition method itself might contribute to this phenomenon, where the layering process could create localized regions of disparate densities due to variances in material flow and settling behaviors. This would affect the internal structure, giving rise to a pattern of porosity that is not consistent throughout the same plane.

3.2. Tensile properties

Fig. 4a presents the longitudinal tensile stress-strain curves, which demonstrate the good repeatability of three specimens. When loaded longitudinally, the SMPCs exhibit extremely high Young's modulus and tensile strength. However, the elongation at break during longitudinal stretching is approximately 0.009, which falls below the average elongation at break of carbon fibers (around 0.015). This discrepancy can be attributed to poor bonding properties at the fiber/matrix interface, stemming from the 3D printing process. This further impedes timely and efficient transfer of loads, thereby causing some defective fibers to fracture prematurely, resulting in specimen failure. When subjected to off-axis loading (Fig. 4b), the load-bearing capacity of SMPC for tensile loads significantly reduces. Both the Young's modulus and tensile

strength gradually decline with increasing fiber off-axis angle θ . Besides, owing to the viscoelastic nature of the SMP matrix, SMPCs exhibit substantial plastic yielding in the stress-strain curve during off-axis stretching.

Fig. 4c presents the statistical histograms depicting the Young's modulus and tensile strength of SMPC specimens with varying fiber off-axis angles at room temperature. As the fiber off-axis angle θ increases from 0° to 30° , the Young's modulus of SMPC decreases by 88.2%, plummeting from 18.94 GPa to 2.24 GPa. Concurrently, the tensile strength exhibits a 76.7% decrease, from 173.7 MPa to 40.4 MPa. Further increases in the fiber off-axis angle from 30° to 45° or 60° result in only slight reduction in both Young's modulus and tensile strength. The microstructures of SMPC specimens with fiber off-axis angles of 45° and 60° at the fracture surface are given in Fig. 4d and Fig. 4e, respectively. It is evident that the fracture surface runs almost parallel to the fiber direction. The primary failure modes observed in SMPC specimens are fiber shear damage, fiber/matrix debonding, and matrix fracture. The obvious river-like pattern on the SMP matrix indicates a brittle fracture. The contact region between fibers and the matrix displays robust interfacial bonding. However, the impregnation of fiber filaments by the matrix in the middle part of the fiber bundle is poor, with only a few matrix components adhering to the extracted fiber filaments. Besides, the observed fiber misalignment significantly impacts the tensile performance of the 4D printed SMPCs. Misaligned fibers do not carry the load efficiently, leading to premature shear failure and debonding at the fiber/matrix interface. This misalignment reduces the composite's effective load-bearing cross-section, thereby diminishing its overall tensile strength and modulus.

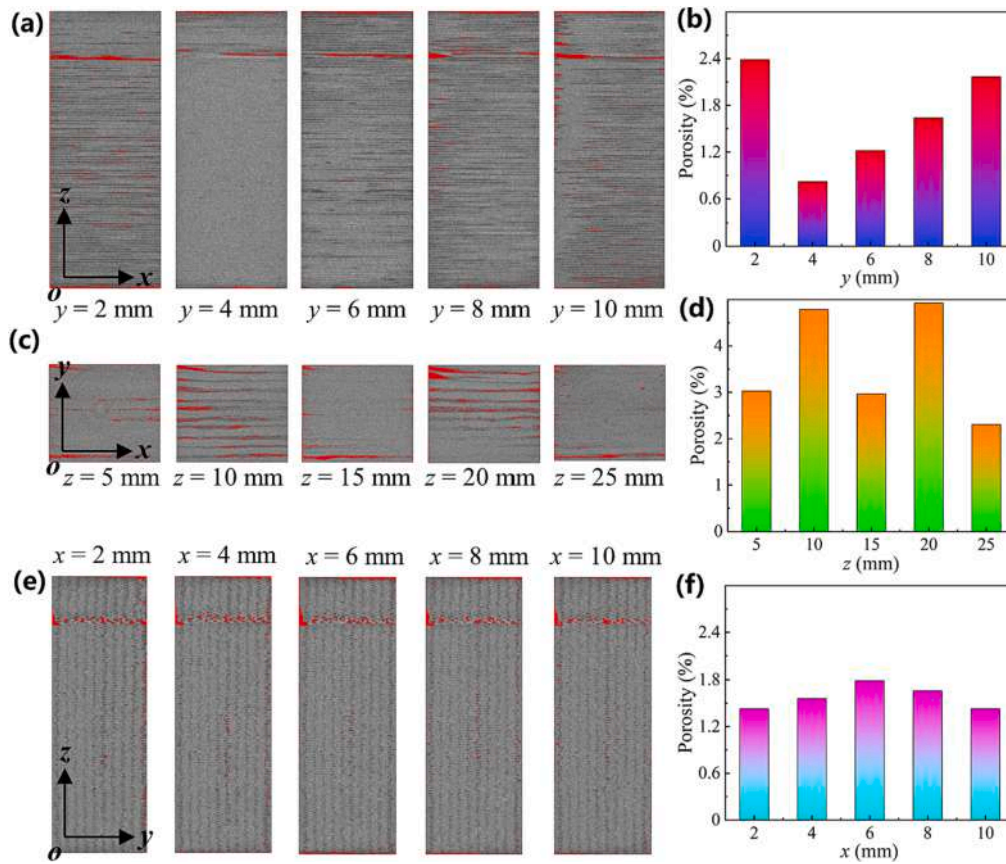


Fig. 3. Void distribution and porosity statistics in different coordinate planes. (a) Void distribution and (b) porosity at various y values in the x - z plane. (c) Void distribution and (d) porosity at various z values in the x - y plane. (e) Void distribution and (f) porosity at various x values in the y - z plane.

3.3. Bending properties

When the fiber off-axis angle θ aligns with the span direction ($\theta = 0^\circ$), the bending stress–strain curve of SMPC follows a linear trend (Fig. 5a). As the fiber off-axis angle increases, the bending stress–strain curve of SMPC gradually deviates from linearity, revealing the onset of plastic yielding behavior (Fig. 5b).

Fig. 5c depicts the statistical distribution of flexural modulus and bending strength for 4D printed SMPCs at varying fiber off-axis angles. The results from three identical specimens exhibit excellent consistency with minimal variation for each specific fiber off-axis angle. Specimens featuring at 0° fiber off-axis angle demonstrate exceptional load-carrying capacity under bending loads, with a bending strength reaching 298.9 MPa, significantly surpassing the tensile strength at the same fiber off-axis angle. This marked disparity in strength can be attributed to the fibers' alignment with the bending load, which allows for optimal stress distribution and resistance to deformation. While tensile forces directly align with the fibers' longitudinal axis, causing potential failure at lower stresses, bending forces introduce a moment that places fibers in compression and tension simultaneously, enabling the material to endure greater stress before reaching its breaking point.

As the fiber off-axis angle increases to 30° , the maximum bending stress drops to 108.9 MPa, representing a reduction of 63.6%. Carbon fibers possess extremely high longitudinal strength, granting SMPC specimens' remarkable resistance to bending when the fiber orientation aligns with the span direction. However, the specimen with a fiber off-axis angle of 0° exhibit a bending strain of approximately 0.024 at the point of maximum bending stress, much lower than the 0.055 exhibited by the specimen with a fiber off-axis angle of 30° , as shown in Fig. 5a and Fig. 5b. Despite the high longitudinal strength of carbon fibers, their limited elongation at break results in lower failure strains under bending

loads for specimens with a fiber off-axis angle of 0° . Fig. 5d reveals asymmetric deformation of the specimen with a fiber off-axis angle of 30° under three-point bending, attributed to anisotropy from unidirectional fiber layup. As loading displacement at the midpoint of the span increases, fibers on the tension side face higher stress, leading to potential failure through matrix cracking or fiber breakage, while the compression side may show fiber buckling or kinking, resulting in an overall non-uniform failure mode.

3.4. Compression properties

Fig. 6a explicates stress–strain curves of the 4D printed SMPC under longitudinal compression with varying fiber volume fractions. These curves reveal that the specimens undergo yield failure after the initial elastic phase, but still maintain some load-bearing capacity after failure. Fig. 6b provides data on the compressive modulus and compressive strength of SMPC specimens with various fiber volume fractions under longitudinal compression. Each volume fraction is tested with three specimens, and the results are averaged. For specimens with fiber volume fractions of 12%, 19%, and 28%, the average longitudinal compressive moduli are 3.95 GPa, 4.80 GPa, and 5.31 GPa, respectively. This demonstrates a gradual increase in longitudinal compressive modulus with higher fiber volume fractions. However, the increase rate in compressive modulus decreases as the fiber volume fraction rises. This decrease can be attributed to the reduced efficiency of stress transfer due to tighter packing and possible defects, as well as the matrix's diminished ability to distribute stress amongst an increasing number of fibers [44]. The undesired reduction in efficiency of stress transfer poses a greater impact on longitudinal compressive strength compared to compressive modulus. It is evident from Fig. 6b that the longitudinal compressive strength of SMPC specimens does not increase

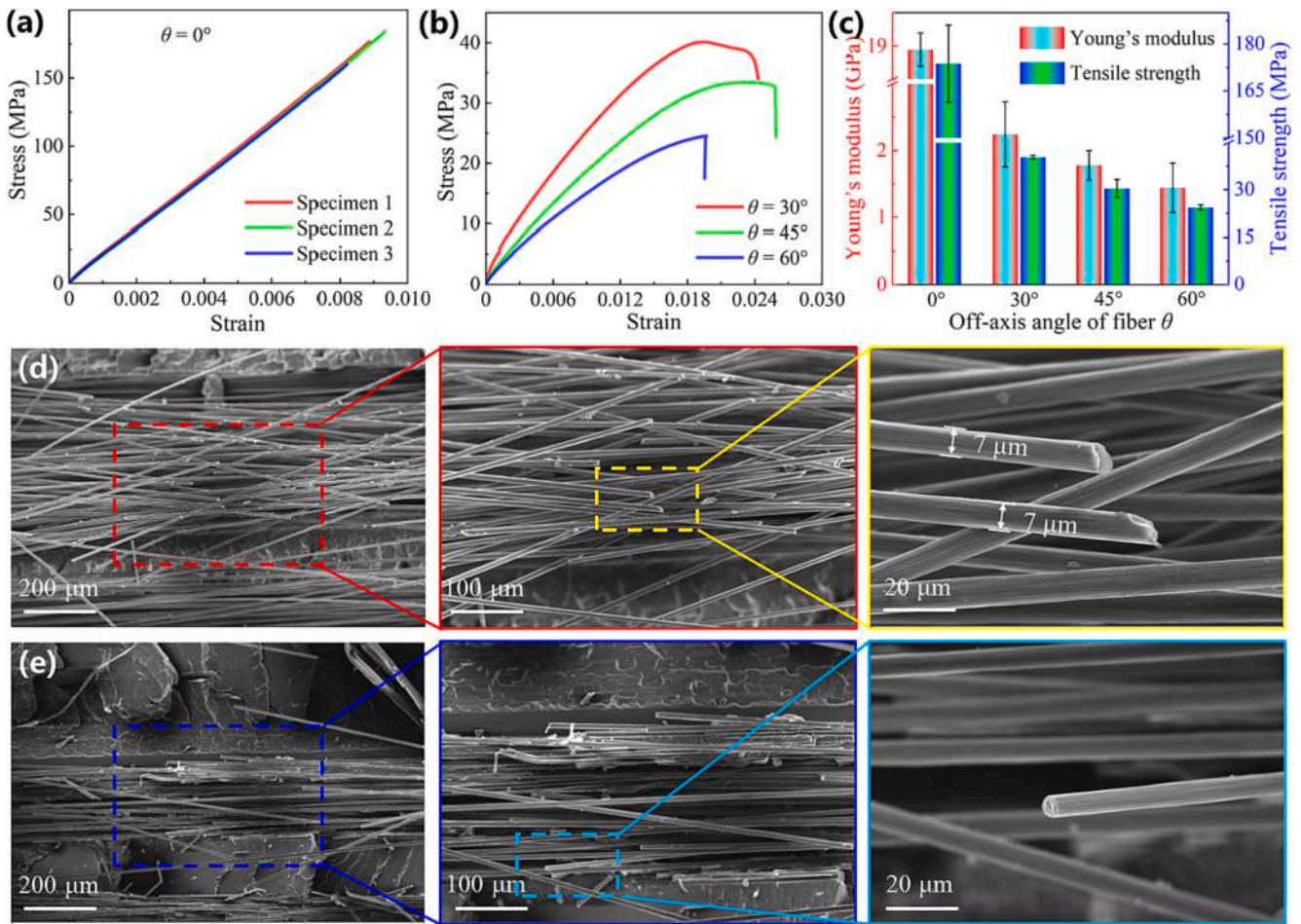


Fig. 4. Tensile mechanical properties of the 4D printed SMPCs. (a) Longitudinal tensile stress–strain curves. (b) Off-axis tensile stress–strain curves. (c) Variations of Young's modulus and tensile strength with fiber off-axis angle θ . Fracture micromorphology of the specimen with an off-axis angle of (d) 45° and (e) 60° .

obviously as the fiber volume fraction goes from 12% to 28%.

Transverse compression tests are conducted in addition to longitudinal compression tests on the 4D printed SMPC specimens, where the compression direction is perpendicular to the fiber direction. Fig. 6c presents the results of transverse compression tests for SMPC specimens with a fiber volume fraction of 12%. These results indicate low dispersion among the test results of three specimens. Notable, the stress–strain curves under transverse compression exhibit a distinct evolution trend compared to longitudinal compression, with specimens displaying obvious plastic deformation. During transverse loading, the SMP matrix, being a viscoplastic polymer, primarily carries the load, leading to plastic yielding in SMPC specimens. The average transverse compressive modulus and strength for SMPC specimens with a fiber volume fraction of 12% are 1.03 GPa and 80.8 MPa, respectively. These values are 73.9% and 38.4% lower than the corresponding values obtained from longitudinal compression.

To better understand the failure mode of the 4D printed SMPC under transverse compression, the stress state in Fig. 6d is defined, where the fracture angle α requires determination. The primary failure of SMPC under transverse compression is matrix failure. Matrix failures, such as shear failure, tensile/compressive failure, and combinations thereof, arise due to in-plane shear stress, out-of-plane shear stress, and transverse normal stress. The behavior of matrix failure is directly influenced by stress components (σ_{mn} , τ_{nl} , and τ_{nl}) on the fracture plane. Fig. 6e gives an image of the SMPC specimen after transverse compression failure, revealing that the fracture plane aligns parallel to the fiber direction. Moreover, a fracture angle of about 45° is ascertained. The local micromorphology on the fracture plane following transverse

compression demonstrates intact fiber pull-out and slight fiber misalignment. Misaligned fibers can cause uneven stress distribution, leading to premature failure in the matrix. This compromises the structural integrity and might reduce the load-bearing capacity of the SMPC. Therefore, controlling fiber orientation during the printing process is critical for optimizing the mechanical and functional properties of SMPCs under compression.

3.5. Shape memory behavior

SMPC specimens, initially fashioned into rectangular geometries (95 mm \times 13 mm \times 2.4 mm), are manufactured with a fiber off-axis angle of 45° . In a 70°C environment, the rectangular specimen is bent by an angle φ to achieve an arc-shaped temporary configuration, which is then set by cooling the specimen (Fig. 7a). Following a procedure similar to the one detailed in Section 2.5 for the shape memory cycle test, corresponding finite element simulations are implemented. Fig. 7b presents the response of the arc-shaped SMPC specimen obtained through finite element simulation concerning temperature, bending moment, and bending angle during the shape memory cycle. During the cooling phase, the bending moment exhibits a J-shaped evolution, reaching a maximum value of 4.17 N.mm at the lowest temperature (25°C). After unloading the bending moment at low temperature, the bending angle remains almost unchanged, signifying a shape fixity rate of nearly 100%. As the temperature increases from 25°C to 80°C , a significant variation in bending angle is observed, suggesting excellent shape recovery performance. Shape recovery initiates when the specimen is heated to 55°C , representing the lower limit of the phase transition temperature

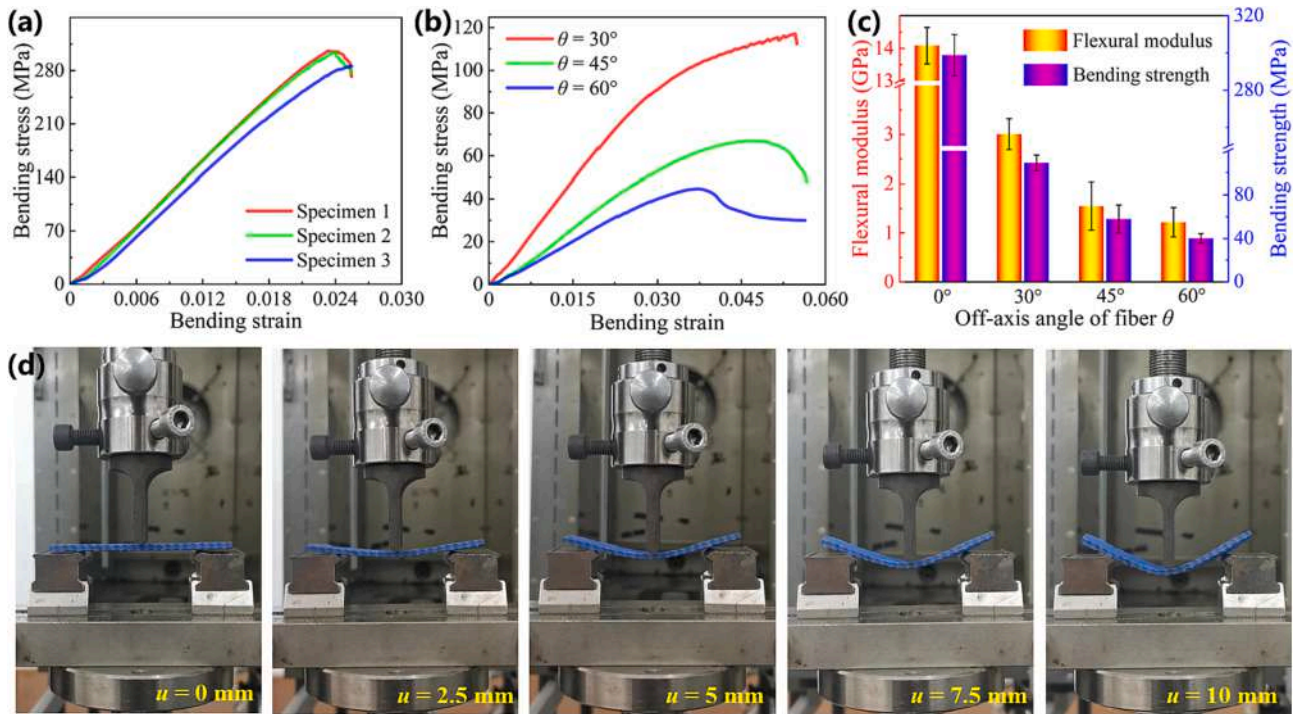


Fig. 5. Bending properties of the 4D printed SMPCs. (a) Bending stress–strain curves of specimens with fiber off-axis angles of 0°. (b) Bending stress–strain curves of specimens with fiber off-axis angles of 30°, 45°, and 60°. (c) Statistics of flexural modulus and bending strength. (d) The deformation process of the specimen with fiber off-axis angle of 30° under three-point bending.

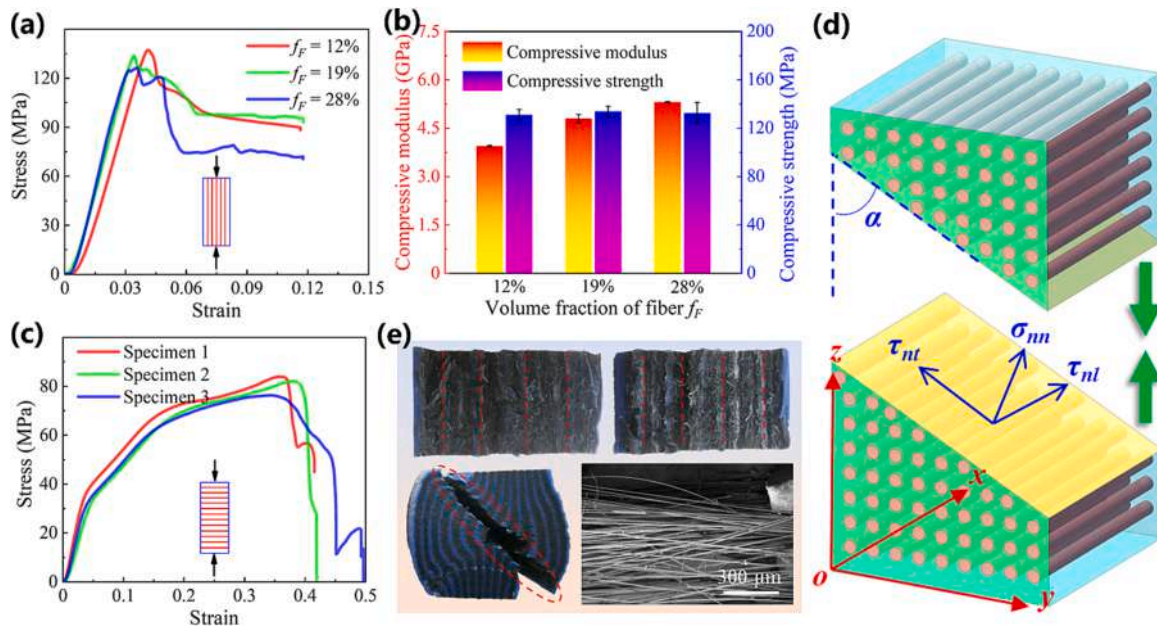


Fig. 6. Compression properties of the 4D printed SMPCs. (a) Longitudinal compressive stress–strain curves of SMPCs with various fiber volume fractions. (b) Modulus and strength under longitudinal compression versus fiber volume fraction f_F . (c) Transverse compressive stress–strain curves of SMPCs with a fiber volume fraction of 12%. (d) Stress state on the failure plane. (e) Failure mode under transverse compression.

region of SMPC. The shape recovery process of the arc-shaped specimen, obtained through both experiments and finite element simulations, is presented in Fig. 7c, revealing good consistency. It is important to note that in the experimental results, the arc-shaped specimen exhibited a shape recovery rate of 96.3%. The shape recovery rate is defined as $Shape\ recovery\ rate = (\theta_i - \theta_e) / \theta_i \times 100\%$, where θ_i and θ_e are the angles before and after recovery, equal to 270° and 10°, respectively. This unrecovered angle is attributed to the original defects and irreversible

plastic deformation in the specimen.

Fig. 7d presents a complex SMPC mesh structure fabricated using the 4D printing technique, characterized by a symmetric fiber lay-up achieved by customizing the movement path of the nozzle. The envelope dimensions of this mesh structure are 92 mm × 80 mm × 0.6 mm, with the relatively small thickness facilitating out-of-plane bending. The mesh structure is bent to an angle of 250° at 70 °C to attain a curved temporary configuration. Fig. 7e illustrates the recovery process of the

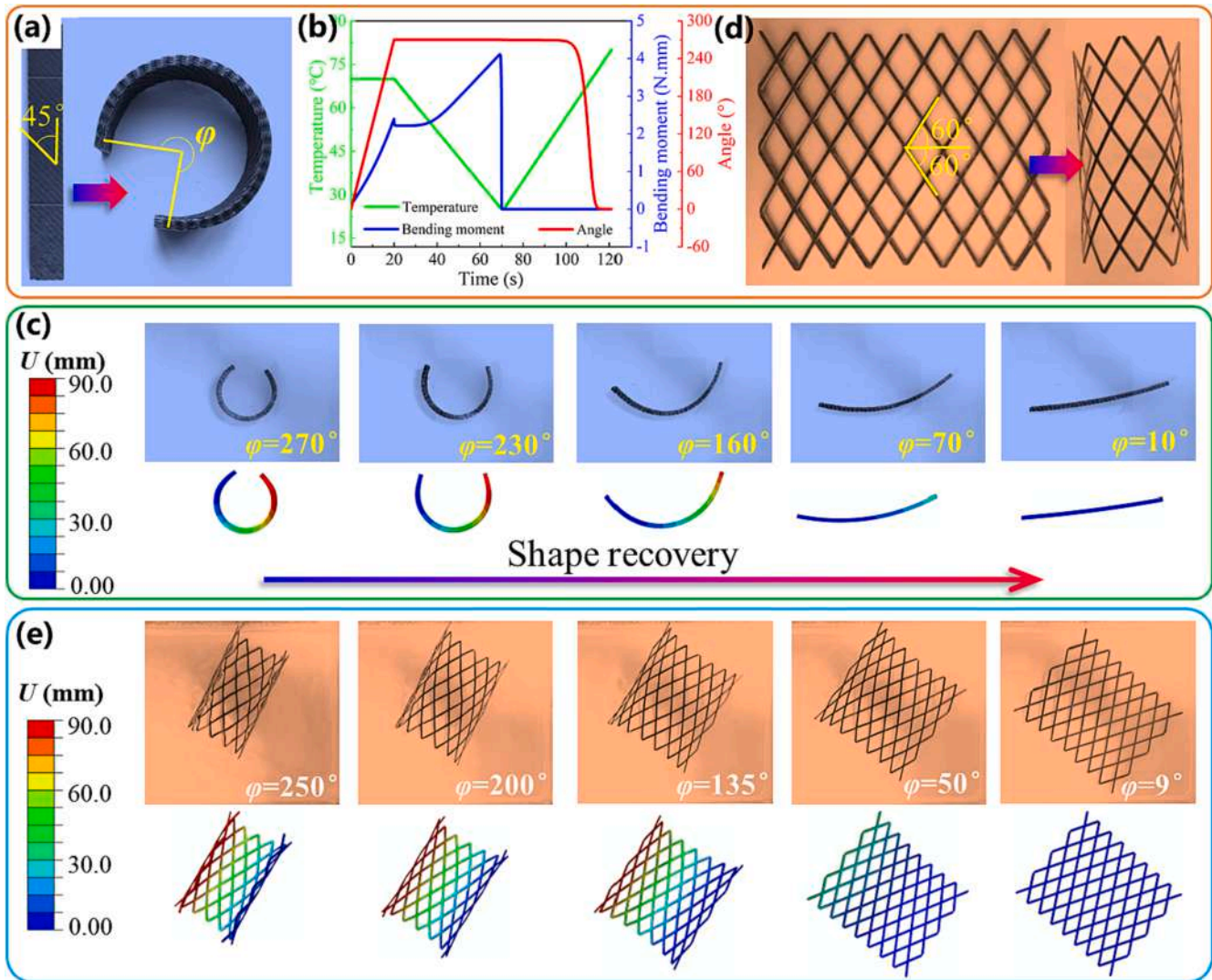


Fig. 7. Shape memory properties of the 4D printed SMPCs. (a) Initial and temporary shapes of the rectangular specimen. (b) Evolution curves of temperature, bending moment, and bending angle of the rectangular specimen over time in the simulation. (c) Experiments and simulations of the shape recovery process for the rectangular specimen. (d) Initial and temporary shapes of the mesh structure. (e) Experiments and simulations of the shape recovery process for the mesh structure.

mesh structure from its temporary shape to the initial shape at elevated temperatures, with finite element simulation providing a satisfactory prediction of the deformation pattern of the structure. Furthermore, a shape recovery rate of 96.4% was obtained from the experimental results. It is noteworthy that the mesh structure presented in this study exhibits a more intricate geometric configuration and deformation pattern compared to the cross-shaped member in previous work [42], demonstrating the versatility of 4D printing in fabricating complex SMPC structures with excellent shape memory effects.

4. Conclusions

Continuous fiber-reinforced SMPCs are produced by a co-extrusion 4D printing process. The micro-CT scanning is employed to characterize the internal void distribution of the 4D printed SMPCs. Layered scanning images and 3D reconstructed images are acquired, revealing that both the coordinate plane and the position of the slice in the thickness direction affected the porosity. Quasi-static tensile, three-point bending, and compression tests are conducted to evaluate the load-bearing capacity of the 4D printed SMPCs against typical mechanical loads. The results demonstrate that the fiber off-axis angle greatly influences the load-bearing capacity of the specimens. For

example, Young's modulus under off-axis loading (fiber off-axis angle of 30°) was 88.2% lower in contrast to that for longitudinal loading (fiber off-axis angle of 0°).

Furthermore, the fiber volume fraction stands as another critical parameter affecting the mechanical properties, with a higher fiber content enhancing the mechanical performance of the 4D printed SMPCs. Nevertheless, excessively high fiber content tends to cause inadequate impregnation between the fibers and the matrix due to the constraints of the printing process. SEM is employed to characterize the fracture morphology of specimens, revealing that matrix failure is the prevailing fracture mode during off-axis loading. Lastly, the shape memory properties of a basic rectangular component and a complex mesh structure are investigated by experiments and finite element simulations. During the experiments and simulations, the deformation sequence under high-temperature stimuli is recorded, which displays typical shape recovery. Shape recovery rates above 96% confirm the substantial application potential of the 4D printed SMPC in smart composites and structures that require both deformability and high load-bearing capacities.

CRedit authorship contribution statement

Chengjun Zeng: Writing – review & editing, Writing – original draft, Visualization, Methodology, Investigation, Funding acquisition, Data curation. **Liwu Liu:** Validation, Resources, Project administration, Methodology, Funding acquisition. **Cheng Lin:** Writing – review & editing, Validation, Methodology. **Xiaozhou Xin:** Writing – review & editing, Validation, Resources, Methodology. **Yanju Liu:** Writing – review & editing, Supervision, Funding acquisition, Conceptualization. **Jinsong Leng:** Writing – review & editing, Supervision, Project administration, Conceptualization.

Declaration of competing interest

The authors declare that they have no known competing financial interests or personal relationships that could have appeared to influence the work reported in this paper.

Data availability

Data will be made available on request.

Acknowledgments

This work was financially supported by the National Natural Science Foundation of China (Grant Nos. 12072094 and 12172106), the China Postdoctoral Science Foundation (Grant No. 2023M730870), the Postdoctoral Fellowship Program of CPSF (Grant No. GZB20230957) and the Heilongjiang Postdoctoral Science Foundation (Grant No. LBH-ZZ3130).

References

- Zhang Q, Dong J, Zhao Y, Zheng Y. Three-dimensional meta-architecture with programmable mechanical properties. *Int J Smart Nano Mater* 2022;13:152–65.
- Shaikeea AJD, Cui H, O'Masta M, Zheng XR, Deshpande VS. The toughness of mechanical metamaterials. *Nat Mater* 2022;21(3):297–304.
- Wang Y, Jin J, Lu Y, Mei D. 3D printing of liquid metal based tactile sensor for simultaneously sensing of temperature and forces. *I Int J Smart Nano Mater* 2021;12:269–85.
- Skylar-Scott MA, Mueller J, Visser CW, Lewis JA. Voxelated soft matter via multimaterial multinozzle 3D printing. *Nature* 2019;575:330–5.
- Lin X, Pan F, Yang K, Guan J, Ding B, Liu Y, et al. A stair-building strategy for tailoring mechanical behavior of re-customizable metamaterials. *Adv Funct Mater* 2021;31(37):2101808.
- Wychowanec JK, Brougham DF. Emerging magnetic fabrication technologies provide controllable hierarchically-structured biomaterials and stimulus response for biomedical applications. *Adv Sci* 2022;9(34):e2202278.
- Wang Z, Ren J, Liu R, Sun X, Huang D, Xu W, et al. Three dimensional core-shell structured liquid metal/elastomer composite via coaxial direct ink writing for electromagnetic interference shielding. *Compos A Appl Sci Manuf* 2020;136:105957.
- Pei H, Jing J, Chen Y, Guo J, Chen N. 3D printing of PVDF-based piezoelectric nanogenerator from programmable metamaterial design: promising strategy for flexible electronic skin. *Nano Energy* 2023;109:108303.
- Howard GD, Brett J, O'Connor J, Letchford J, Delaney GW. One-Shot 3D-printed multimaterial soft robotic jamming grippers. *Soft Robot* 2022;9(3):497–508.
- Tang J, Kwan TH, Wu X. Extrusion and thermal control design of an on-orbit 3D printing platform. *Adv Space Res* 2022;69(3):1645–61.
- Carrola M, Asadi A, Zhang H, Papageorgiou DG, Bilotti E, Koerner H. Best of both worlds: synergistically derived material properties via additive manufacturing of nanocomposites. *Adv Funct Mater* 2021;31:2103334.
- Ren H, Yang X, Wang Z, Xu X, Wang R, Ge Q, et al. Smart structures with embedded flexible sensors fabricated by fused deposition modeling-based multimaterial 3D printing. *Int J Smart Nano Mater* 2022;13(3):447–64.
- Dong X, Zhang F, Wang L, Liu Y, Leng J. 4D printing of electroactive shape-changing composite structures and their programmable behaviors. *Compos A Appl Sci Manuf* 2022;157:106925.
- Zeng C, Liu L, Bian W, Leng J, Liu Y. Compression behavior and energy absorption of 3D printed continuous fiber reinforced composite honeycomb structures with shape memory effects. *Addit Manuf* 2021;38:101842.
- Simunec DP, Breedon M, Muhammad FUR, Kyratzis L, Sola A. Electrical capability of 3D printed unpoled polyvinylidene fluoride (PVDF)/thermoplastic polyurethane (TPU) sensors combined with carbon black and barium titanate. *Addit Manuf* 2023;73:103679.
- Dong K, Wang Y, Wang Z, Qiu W, Zheng P, Xiong Y. Reusability and energy absorption behavior of 4D printed continuous fiber-reinforced auxetic composite structures. *Compos A Appl Sci Manuf* 2023;169:107529.
- Rajabasadi F, Moreno S, Fichna K, Aziz A, Appelhans D, Schmidt OG, et al. Multifunctional 4D-printed sperm-hybrid microcarriers for assisted reproduction. *Adv Mater* 2022;34:2204257.
- Gladman AS, Matsumoto EA, Nuzzo RG, Mahadevan L, Lewis JA. Biomimetic 4D printing. *Nat Mater* 2016;15(4):413–8.
- Huang X, Panahi-Sarmad M, Dong K, Cui Z, Zhang K, Gelis Gonzalez O, et al. 4D printed TPU/PLA/CNT wave structural composite with intelligent thermal-induced shape memory effect and synergistically enhanced mechanical properties. *Compos A Appl Sci Manuf* 2022;158:106946.
- Zeng C, Liu L, Du Y, Yu M, Xin X, Liu T, et al. A shape-memory deployable subsystem with a large folding ratio in china's tianwen-1 mars exploration mission. *Eng* 2023;28:52–60.
- Wang L, Zhang F, Du S, Leng J. 4D printing of shape-changing structures based on IPN epoxy composites formed by UV post-curing and γ -ray radiation. *Compos A Appl Sci Manuf* 2022;162:107146.
- Zhang H, Hong E, Chen X, Liu Z. Machine learning enables process optimization of aerosol jet 3D printing based on the droplet morphology. *ACS Appl Mater Interfaces* 2023;15:14532–45.
- Ren L, Wang Z, Ren L, Liu Q, Li W, Song Z, et al. 4D printing of shape memory composites with remotely controllable local deformation. *Mater Today Chem* 2023;29:101470.
- Ge Q, Sakhaei AH, Lee H, Dunn CK, Fang NX, Dunn ML. Multimaterial 4D printing with tailorable shape memory polymers. *Sci Rep* 2016;6:31110.
- Zhang B, Li H, Cheng J, Ye H, Sakhaei AH, Yuan C, et al. Mechanically robust and UV-curable shape-memory polymers for digital light processing based 4D printing. *Adv Mater* 2021;33:e2101298.
- Xin X, Liu L, Liu Y, Leng J. 4D printing auxetic metamaterials with tunable, programmable, and reconfigurable mechanical properties. *Adv Funct Mater* 2020;30:2004226.
- Spiegel CA, Hackner M, Bothe VP, Spatz JP, Blasco E. 4D printing of shape memory polymers: from macro to micro. *Adv Funct Mater* 2022;32:2110580.
- Yamamura S, Iwase E. Hybrid hinge structure with elastic hinge on self-folding of 4D printing using a fused deposition modeling 3D printer. *Mater Des* 2021;203:109605.
- Tao R, Ji L, Li Y, Wan Z, Hu W, Wu W, et al. 4D printed origami metamaterials with tunable compression twist behavior and stress-strain curves. *Compos Part B Eng* 2020;201:108344.
- Cortés A, Cosola A, Sangermano M, Campo M, González Prolongo S, Pirri CF, et al. DLP 4D-printing of remotely, modularly, and selectively controllable shape memory polymer nanocomposites embedding carbon nanotubes. *Adv Funct Mater* 2021;31:2106774.
- Chacón JM, Caminero MA, Núñez PJ, García-Plaza E, García-Moreno I, Reverte JM. Additive manufacturing of continuous fibre reinforced thermoplastic composites using fused deposition modelling: effect of process parameters on mechanical properties. *Compos Sci Technol* 2019;181:107688.
- Mei H, Ali Z, Ali I, Cheng L. Tailoring strength and modulus by 3D printing different continuous fibers and filled structures into composites. *Adv Compos Hybrid Mater* 2019;2(2):312–9.
- Zhou Y, Yang Y, Jian A, Zhou T, Tao G, Ren L, et al. Co-extrusion 4D printing of shape memory polymers with continuous metallic fibers for selective deformation. *Compos Sci Technol* 2022;227:109603.
- Zeng C, Liu L, Bian W, Liu Y, Leng J. 4D printed electro-induced continuous carbon fiber reinforced shape memory polymer composites with excellent bending resistance. *Compos Part B Eng* 2020;194:108034.
- Le Duigou A, Chabaud G, Scarpa F, Castro M. Bioinspired electro-thermo-hygro reversible shape-changing materials by 4D printing. *Adv Funct Mater* 2019;29:1903280.
- Tian X, Wang Q, Li D. Design of a continuous fiber trajectory for 4D printing of thermally stimulated composite structures. *Sci China Technol Sci* 2020;63:571–7.
- Wang Q, Tian X, Huang L, Li D, Malakhov AV, Polillo AN. Programmable morphing composites with embedded continuous fibers by 4D printing. *Mater Des* 2018;155:404–13.
- de Kergariou C, Kim BC, Perriman A, Le Duigou A, Guessasma S, Scarpa F. Design of 3D and 4D printed continuous fibre composites via an evolutionary algorithm and voxel-based finite elements: application to natural fibre hygromorphs. *Addit Manuf* 2022;59:103144.
- Dong K, Panahi-Sarmad M, Cui Z, Huang X, Xiao X. Electro-induced shape memory effect of 4D printed auxetic composite using PLA/TPU/CNT filament embedded synergistically with continuous carbon fiber: a theoretical & experimental analysis. *Compos Part B Eng* 2021;220:108994.
- Le Duigou A, Fruleux T, Matsuzaki R, Chabaud G, Ueda M, Castro M. 4D printing of continuous flax-fibre based shape-changing hygromorph biocomposites: towards sustainable metamaterials. *Mater Des* 2021;211:110158.
- Lin C, Liu L, Liu Y, Leng J. 4D printing of bioinspired absorbable left atrial appendage occluders: a proof-of-concept study. *ACS Appl Mater Interfaces* 2021;13:12668–78.

- [42] Zeng C, Liu L, Hu Y, Bian W, Leng J, Liu Y. A viscoelastic constitutive model for shape memory polymer composites: Micromechanical modeling, numerical implementation and application in 4D printing. *Mech Mater* 2022;169:104301.
- [43] Zhang Z, Long Y, Yang Z, Fu K, Li Y. An investigation into printing pressure of 3D printed continuous carbon fiber reinforced composites. *Compos A Appl Sci Manuf* 2022;162:107162.
- [44] Hou Z, Tian X, Zheng Z, Zhang J, Zhe L, Li D, et al. A constitutive model for 3D printed continuous fiber reinforced composite structures with variable fiber content. *Compos Part B Eng* 2020;189:107893.